



Kent Academic Repository

Du, Juan, Phillips, Anthony E., Arnold, Donna C., Keen, David A., Tucker, Matthew G. and Dove, Martin T. (2019) *Structural study of bismuth ferrite (BiFeO₃) by neutron total scattering and the reverse Monte Carlo method.* Physical Review B, 100 (10). ISSN 2469-9950.

Downloaded from

<https://kar.kent.ac.uk/77584/> The University of Kent's Academic Repository KAR

The version of record is available from

<https://doi.org/10.1103/PhysRevB.100.104111>

This document version

Author's Accepted Manuscript

DOI for this version

Licence for this version

UNSPECIFIED

Additional information

Versions of research works

Versions of Record

If this version is the version of record, it is the same as the published version available on the publisher's web site. Cite as the published version.

Author Accepted Manuscripts

If this document is identified as the Author Accepted Manuscript it is the version after peer review but before type setting, copy editing or publisher branding. Cite as Surname, Initial. (Year) 'Title of article'. To be published in *Title of Journal*, Volume and issue numbers [peer-reviewed accepted version]. Available at: DOI or URL (Accessed: date).

Enquiries

If you have questions about this document contact ResearchSupport@kent.ac.uk. Please include the URL of the record in KAR. If you believe that your, or a third party's rights have been compromised through this document please see our [Take Down policy](https://www.kent.ac.uk/guides/kar-the-kent-academic-repository#policies) (available from <https://www.kent.ac.uk/guides/kar-the-kent-academic-repository#policies>).

Structural study of bismuth ferrite, BiFeO_3 , by neutron total scattering and the Reverse Monte Carlo method

Juan Du and Anthony E Phillips

School of Physics and Astronomy, Queen Mary University of London, Mile End Road, London, E1 4NS, UK

Donna C Arnold

School of Physical Sciences, University of Kent, Canterbury, Kent, CT2 7NH

David A Keen

ISIS Facility, Rutherford Appleton Laboratory, Harwell Campus, Didcot, Oxfordshire, OX11 0QX, UK

Matthew G Tucker

*Oak Ridge National Laboratory, Neutron Scattering Division,
1 Bethel Valley Road, Oak Ridge, TN 37831, USA*

Martin T Dove*

*Department of Physics, School of Sciences, Wuhan University of Technology,
205 Luoshi Road, Hongshan district, Wuhan, Hubei, 430070, People's Republic of China;
College of Computer Science and College of Physical Science & Technology,
Sichuan University, Chengdu 610065, People's Republic of China; and
School of Physics and Astronomy, Queen Mary University of London, Mile End Road, London, E1 4NS, UK*

We report a study of the atomic structure of the multiferroic material bismuth ferrite, BiFeO_3 , using neutron total scattering measurements coupled with analysis using the Reverse Monte Carlo method. We have examined average neighbouring interatomic distances and local coordination environments, together with their fluctuations, for temperatures between 16–800 K (the sample decomposed at higher temperatures). There is little change in the average structure as a function of temperature, but the results show unusually large thermal motion at higher temperatures. No anomalous behaviour is seen within this range, suggesting that the anomalies reported to occur below room temperature most likely arise due to effects associated with surfaces and interfaces.

I. INTRODUCTION

Bismuth ferrite, BiFeO_3 , is the most widely studied multiferroic ceramic, primarily because it exhibits both magnetic ($T_N \sim 630$ K) and ferroelectric ($T_C \sim 1100$ K) ordering at room temperature¹. BiFeO_3 has the perovskite structure, with the Fe^{3+} cation occupying the octahedral site and the Bi^{3+} cation on the cuboctahedral sites coordinated to 12 oxygen anions, as shown in Figure 1.

At room temperature bismuth ferrite crystallises in the α -phase with rhombohedral symmetry, polar space group $R3c$, with the FeO_6 octahedra rotated in an antiphase arrangement about the rhombohedral 3-fold axis (Glazer notation $a^-a^-a^-$). Both cations are displaced from the centre of symmetry along the $[001]_h$ axis of the hexagonal unit cell (corresponding to the $[111]_c$ axis of the parent cubic phase)^{1,2}, with the Bi^{3+} displacement being largest due to the stereo-active lone pair. Below T_N the magnetic moments of Fe^{3+} order into a complex long-range incommensurate spin cycloid propagating in the $[110]_h$ direction with a periodicity of approximately 620 Å.³ It is now generally accepted that at T_C BiFeO_3 undergoes a first-order phase transition to an orthorhombic β -phase with non-polar $Pbnm$ symmetry⁴.

Above 1198 K BiFeO_3 adopts the γ -phase, the sym-

metry of which continues to be debated. Initially it was suggested that γ - BiFeO_3 adopts the aristotype cubic perovskite $Pm\bar{3}m$ symmetry⁵. However, neutron diffraction experiments suggest that the γ -phase may retain orthorhombic symmetry⁶. High temperature studies are usually compromised as a result of the thermal instability of BiFeO_3 . It has been demonstrated that the expected decomposition products are marginally more thermally dynamically stable in the temperature range 720–1040 K^{7,8}. More recently differential scanning calorimetry measurements have suggested that BiFeO_3 is kinetically unstable above T_C with the β - γ phase transition overlapping the peritectic decomposition⁹. It was also suggested that the structural phase transitions are interlinked and kinetically controlled, and thus dependent on the heating rate. As a result the onset of decomposition of BiFeO_3 can occur significantly below the peritectic decomposition temperature, and is somewhat dependent on experimental conditions. This is consistent with the difficulty to obtain a pure γ -phase in diffraction experiments⁴⁻⁶.

Inelastic neutron spectroscopy experiments conducted between 200–750 K exhibited a broadening of the whole excitation spectrum with increasing temperature, which was interpreted in terms of large-amplitude anharmonic motions of Bi and O ions¹¹. An anomaly in the Bi-dominated modes around T_N was interpreted as strong evidence for spin-phonon coupling. A more recent in-

elastic study performed between 300–700 K revealed no significant changes in the dynamic response with temperature¹², although broadening of the energy line widths on heating towards T_N was observed as in reference 11, leading to the suggestion that the low-energy lattice dynamics and magnetic order are coupled^{11,12}.

The low temperature behaviour of BiFeO_3 remains the subject of much debate within the literature. No significant changes in the long-range nuclear (atomic) or magnetic structures with varying temperature have been reported in crystallographic studies of single crystal and powder samples of the bulk phases^{4,13,14}. On the other hand, anomalous features have been reported in the Raman spectra at multiple temperatures between 140–250 K^{1,15–17}. Since crystallographic measurements are sensitive to the average structure of the bulk material, there are broadly two possible explanations for this discrepancy. Firstly, many of these studies rely on point analysis of Raman spectra. The position and intensity of a particular mode can be critically dependent on the domain orientation such that features may not necessarily arise as a result of temperature dependence but rather experimental control^{2,18}. Alternatively these anomalies may not be due to the bulk structure at all, and instead may arise from grain boundaries with polar character or from the existence of surface phase transitions¹⁹. Indeed, Domingo et al. have suggested the presence of a 5 nm surface and a subsurface layer with a thickness of around 320 nm, both of which behave differently, electrically and structurally, to the bulk^{20,21}. Second, the *local* structure may be more complex than the crystallographic average structure suggests. A recent neutron diffraction and in-

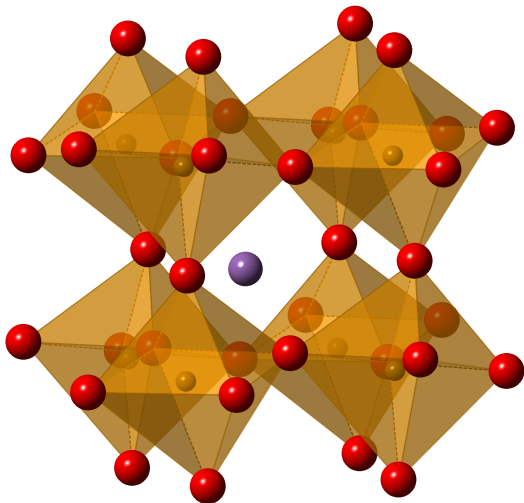


FIG. 1. Structural representation of BiFeO_3 in the polar α -phase with space group $R3c$. The Fe ions and FeO_6 octahedra are represented by the brown spheres and polyhedra respectively, and the oxygen and bismuth ions are shown as red and purple spheres respectively. Structure diagrams in this paper were generated with the CrystalMaker software¹⁰.

elastic scattering study on BiFeO_3 nanomaterials²² suggests that the FeO_6 octahedra become more anisotropic over a narrow range of temperatures around 205 K. Small concomitant changes in the magnetic sublattice were attributed to a spin rearrangement; the inelastic scattering data show anomalies in the widths of the magnetic features, indicative of slow spin dynamics below 205 K.

One way to approach this puzzle is to investigate the local structure of BiFeO_3 directly. To date local structure studies have primarily been limited to room temperature X-ray absorption spectroscopy and X-ray pair distribution function (PDF) performed as part of comparative doping studies^{23–29}. PDF studies at room temperature have been performed on BiFeO_3 – PbTiO_3 solid solutions³⁰ and La/Tb-doped BiFeO_3 ²⁵. However, up to now no variable temperature PDF studies have been performed on undoped BiFeO_3 .

In this paper we describe a variable-temperature neutron PDF study of undoped BiFeO_3 with analysis using the Reverse Monte Carlo (RMC) method. This approach, uniquely, is able to give simultaneous information about average crystal structure and local fluctuations in the atomic arrangement. The key objective of this work is to examine fluctuations in the structure across the temperature range from 16–800 K, particularly to see if these show any signs of the various anomalies previously reported, and to explore any possible link between magnetism and ferroelectricity. Unfortunately, whilst this temperature range encompasses T_N , it falls short of T_C due to problems of sample stability. Nevertheless, the results here show robustly the growth of large structural fluctuations whilst the average structure remains surprisingly constant and consistent across the whole temperature range. We will show that neither the average structure nor the local fluctuations show features that reflect the previously-reported anomalies or changes in the magnetic order.

II. EXPERIMENTAL METHODS AND DATA ANALYSIS

A. Experimental procedures: sample and neutron scattering measurements

BiFeO_3 was synthesised using the same methods we have previously reported^{6,31}. Briefly, stoichiometric ratios of Bi_2O_3 (Sigma Aldrich, 99.9% purity) and Fe_2O_3 (Sigma Aldrich, purity above 99%) were ground together thoroughly. A 6 mol% excess of Bi_2O_3 was added in order to mitigate against the loss of bismuth during the reaction. The material was heated to 800 °C with a heating rate 10 °C/min, and held at this temperature for 5 hours. The resulting powder was leached in 2.5 M HNO_3 with continuous stirring before being washed with double-distilled H_2O and dried at 400 °C (1 hour). Phase purity was confirmed by powder diffraction using a Bruker D8 Advance diffractometer using $\text{Cu K}\alpha_1$ radi-

tion (40 kV and 40 mA, $\lambda = 1.5406 \text{ \AA}$, 2θ range $10\text{--}70^\circ$).

Neutron total scattering measurements were performed using the GEM instrument at the ISIS spallation neutron scattering facility³². This provides high-quality data to high values of Q , up to 50 \AA^{-1} , although oscillations in $i(Q)$ had already decayed by smaller values of Q as seen in data shown later in this paper. High values of Q permit better resolution for the structural models in real space, with resolution given as $\Delta r = 2\pi/Q_{\text{max}}$. The range of Q available to the experiment corresponds to a practical range of neutron wavelengths of $0.15\text{--}2 \text{ \AA}$, which enables energy transfers that correspond to a full integration over all energy transfers implicit in the formulation of the scattering function $i(Q)$ from the full dynamical scattering factor. Thus the configurations in the RMC analysis will be sensitive to the full range of phonon excitations in BiFeO_3 .

The powder sample was loaded into a cylindrical vanadium can of 8 mm diameter. Total scattering data were obtained in two rounds of experiments performed at different times. The first round enabled data collection at temperatures of 16 K, 96 K, 161 K, 236 K, 283 K with the sample in a closed-cycle refrigerator (CCR), and, 294 K, 600 K and 700 K with the sample in a furnace³³. The second round enabled data collection at temperatures of 291 K, 373 K, 473 K, 572 K, 627 K, 662 K and 798 K in a furnace³⁴. Measurement times at each temperature were around 6 hours, corresponding to a total proton flux of around $900 \mu\text{A hr}$.

We found that the nominal temperature of 800 K was the highest temperature we could achieve in these experiments. With the long run times required for these measurements, together with holding the sample in a vacuum rather than air, heating above 800 K led to the formation of decomposition products (such as $\text{Bi}_2\text{Fe}_4\text{O}_9$), as seen in the diffraction data. This is not unusual in BiFeO_3 as has been discussed elsewhere^{7,8}. The sample was replaced by a fresh sample taken from the same synthesis batch for subsequent measurements after the first signs of decomposition; diffraction data showed no decontamination products in any of the data sets analysed and presented here.

Data were also collected in each round on an empty instrument, then with the sample environment equipment without sample can, and finally with the sample environmental equipment with an empty sample can, in order to account for additional scattering processes and beam attenuation. A long measurement of the scattering from a vanadium rod was performed for data normalisation and calibration of the instrument detectors.

B. Rietveld refinement

The raw diffraction data were processed to form a set of data for Rietveld refinement using the MANTID software³⁵. Rietveld refinement on the data was performed using the GSAS software³⁶ with the EXPGUI

interface³⁷.

The refinements were performed using GSAS lineshape 2 (see the manual³⁶ for explanation). Instrumental parameters used in the refinement were taken from in-house calibration runs. There is, however, a problem with using three different datasets (one with the CCR, two with furnaces) in that in each case the sample position is slightly displaced from the centre in a different way. This has a small but noticeable effect on the refined lattice parameters. In fact GSAS has a parameter to account for this (called ‘‘DIFC’’). To bring the three datasets into consistency we followed the strategy of refining profile parameters associated with the sample at the lowest-temperature data and then holding these fixed in the refinements of all other data. We then compared the three data sets around room temperature. The lattice parameters for the two room-temperature measurements in the furnace were taken from the refinements of the CCR data (using a simple polynomial fit to the data to enable extrapolation to the actual temperatures to account for the small differences in temperature between three data sets at nominally room temperature). Keeping the lattice parameter fixed, the sample displacement parameter was refined, and this was then held fixed in the refinements of higher-temperature data.

C. Total scattering and the Reverse Monte Carlo method

The total scattering structure factor $i(Q)$ was obtained from the total scattering data after correcting for scattering and attenuation by the sample can and sample environment, and the detectors normalised by the measurement of incoherent scattering from the vanadium rod. We used the GUDRUN code³⁸ for this task. The maximum value of Q in the data processing was set to be 40 \AA^{-1} for all the temperatures.

The structure factor is related to the partial atomic pair distribution functions $g_{mn}(r)$ through the standard relation:

$$i(Q) = 4\pi\rho \int_0^\infty \sum_{m,n} c_m c_n b_m b_n r^2 (g_{mn}(r) - 1) \frac{\sin(Qr)}{Qr} dr \quad (1)$$

where $g_{mn}(r)$ is defined such that the number of atoms of type n lying within a spherical shell of radius r and thickness dr centred on an atom of type m is equal to $4\pi c_n \rho r^2 g_{mn}(r)$, with ρ denoting the total number of atoms per unit volume, and c_n denoting the fraction of all atoms of type n . We define the overall pair distribution function as

$$D(r) = 4\pi\rho r \sum_{m,n} c_m c_n b_m b_n (g_{mn}(r) - 1) \quad (2)$$

The functions $i(Q)$ and $D(r)$ are linked through a pair of Fourier sine transforms, which follow from the above

definitions:

$$Qi(Q) = \int_0^\infty D(r) \sin(Qr) dr \quad (3)$$

and

$$D(r) = \frac{2}{\pi} \int_0^\infty Qi(Q) \sin(Qr) dr \quad (4)$$

$D(r)$ is our function of choice to represent the pair distribution function, in part because as the direct Fourier transform from the analysis presented in the above equations the errors will propagate more-or-less uniformly across the transform, and in part because $D(r)$ emphasises the higher- r data more than the functions $g_{mn}(r)$ as a result of the multiplicative factor of r . Although GUDRUN can generate the $D(r)$ function, in this work we performed the Fourier transforms using the STOG program from the ATLAS data analysis suite³⁹, in part because we chose to use a modification function in the Fourier transform to reduce the effect of termination ripples associated with a finite maximum value of Q , Q_{\max} , and to reduce the effects of noise in $Qi(Q)$ at high Q . Thus our transform is

$$D(r) = \frac{2}{\pi} \int_0^{Q_{\max}} M(Q) Qi(Q) \sin(Qr) dr \quad (5)$$

where, following the procedure proposed by Lorch^{40,41}, $M(Q) = \sin(\pi Q/Q_{\max})/(\pi Q/Q_{\max})$.

We should comment about the role of magnetic scattering. Because the magnetic part of the Fe atoms are in the outer atomic shells, the value of the magnetic form factor decreases quickly with Q . For the same reason, without any special attention peaks in the PDF from magnetic correlations will be extremely broad and essentially indistinct. By not accounting for magnetic scattering within the reduction of the total scattering data, corrections to make the data consistent with the known density and atomic composition (that is, to give the expected slopes in the low- Q and low- r parts of the $Qi(Q)$ and $D(r)$ functions respectively), the data reduction method will have treated the magnetic diffuse scattering as noise and subtracted it from the final form of the $i(Q)$ function. The only part of the final data sets therefore that will contain magnetic scattering is the Bragg profile, where there is one strong magnetic peak that could easily be excluded from the RMC analysis and some much weaker peaks.

RMC modelling was performed using the RMCprofile program⁴², which is optimised for applying the method to crystalline materials. The method uses the traditional Metropolis Monte Carlo algorithm to move atoms, using an ‘energy’ function that reflects the agreement between calculated and measured functions $i(Q)$, $D(r)$ and the Bragg profile. Specifically, writing the measured (observed) and calculated value of any function at data point i in data-set j as $y_{i,j}^{\text{obs}}$ and $y_{i,j}^{\text{calc}}$ respectively, we define the function

$$\chi^2 = \sum_j \sum_i (y_{i,j}^{\text{obs}} - y_{i,j}^{\text{calc}})^2 / \sigma_j \quad (6)$$

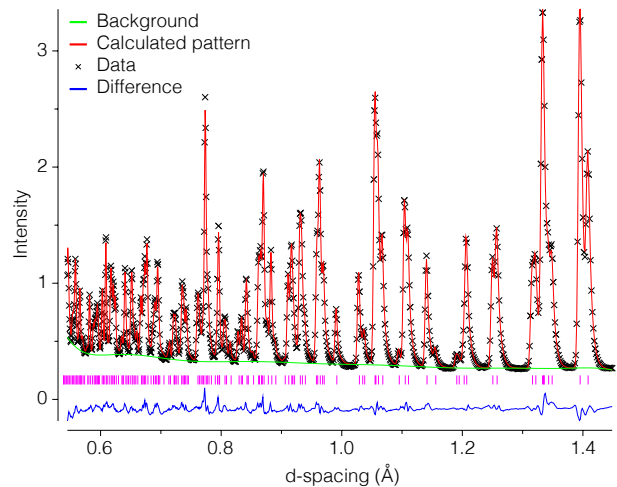


FIG. 2. Example of the quality of the Rietveld refinement of the crystal structure of BeFeO_3 from data collected in this study. Here we show a portion of the data from the 90° bank at a temperature of 161 K. Positions of Bragg reflections are shown as the short vertical magenta lines.

where σ_j provides a weighting for a specific data-set and represents the statistical accuracy of the data set, albeit not on a point-by-point basis. Atomic moves are proposed at random (random atom, random movement subject to a maximum value of the atomic displacement). A move that lowers the value of χ^2 is accepted, but a move that raises the value of χ^2 by an amount $\Delta\chi^2$ is accepted with probability $\exp(-\Delta\chi^2/2)$. In order to prevent atoms moving too far away from their local topology within the crystal structure, we employed distance windows, which impose a minimum and maximum atomic separation between pairs of atoms defined by a prior neighbour list.⁴³

The supercell configurations were set up with orthogonal edge sizes of around 48 Å, 50 Å and 56 Å, containing 10800 atoms; this was a $5 \times 9 \times 4$ supercell of the C -centred orthorhombic cell obtained by transformation of the hexagonal unit cell, with lattice vectors $2\mathbf{a}_h + \mathbf{b}_h, \mathbf{b}_h, \mathbf{c}_h$. The starting positions were generated directly from the crystal structures generated by Rietveld refinement. Each RMC analysis was run for long enough to give more than 200 accepted moves per atom. Maximum atomic moves were of size 0.05 Å. Convergence of the RMC simulations was checked by monitoring the value of χ^2 as defined above.

III. AVERAGE STRUCTURE FROM RIETVELD REFINEMENT

Rietveld refinement of data collected over the whole temperature range measured showed an excellent fit to the $R3c$ model consistent with previous studies^{4,14,44}. A sample fit to the data, namely for the data at 161 K, is shown in Figure 2.

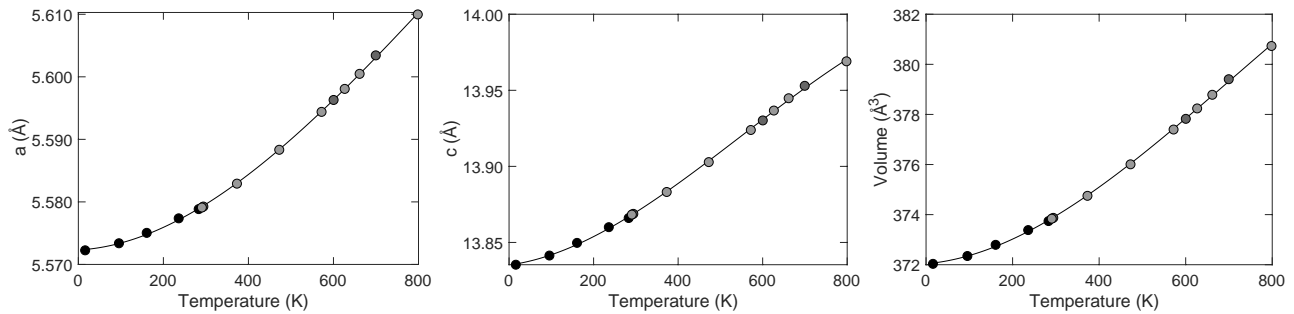


FIG. 3. The refined lattice parameters of BiFeO_3 as functions of temperature from Rietveld refinement of the data obtained in this study. Different fill colours for the data points reflect the different data runs. The curves are guides to the eye obtained by fitting third-order polynomials; the sigmoidal shape for c is consistent with more extensive data reported previously¹⁴. In each graph the error bars are smaller than the size of the data symbols.

T (K)	a (Å)	c (Å)	Fe z	O x	O y	O z
16 (I)	5.57227(7)	13.8354(3)	0.22031(10)	0.44110(27)	0.01806(30)	0.95165(14)
96 (I)	5.57338(6)	13.8414(3)	0.22029(10)	0.44113(27)	0.01794(30)	0.95166(15)
161 (I)	5.57505(7)	13.8498(3)	0.22034(10)	0.44109(27)	0.01776(31)	0.95174(15)
236 (I)	5.57736(7)	13.8601(3)	0.22041(10)	0.44094(27)	0.01752(31)	0.95186(15)
283 (I)	5.57884(6)	13.8661(3)	0.22051(10)	0.44100(26)	0.01742(30)	0.95197(15)
291 (III)	5.57911(7)	13.8684(3)	0.22073(10)	0.44000(27)	0.01720(31)	0.95243(16)
294 (II)	5.57925(6)	13.8689(3)	0.22056(10)	0.44050(27)	0.01711(31)	0.95214(15)
373 (III)	5.58292(6)	13.8832(3)	0.22099(10)	0.44044(25)	0.01719(29)	0.95276(15)
473 (III)	5.58832(5)	13.9028(2)	0.22131(8)	0.44160(21)	0.01732(25)	0.95305(13)
572 (III)	5.59438(4)	13.9239(2)	0.22162(6)	0.44407(16)	0.01793(19)	0.95323(10)
600 (II)	5.59627(4)	13.9301(2)	0.22155(6)	0.44449(16)	0.01760(18)	0.95301(9)
627 (III)	5.59805(3)	13.9366(1)	0.22170(5)	0.44671(13)	0.01863(15)	0.95307(8)
662 (III)	5.60045(3)	13.9446(1)	0.22179(5)	0.44838(13)	0.01906(15)	0.95302(7)
700 (II)	5.60339(3)	13.9528(1)	0.22189(5)	0.44789(14)	0.01851(16)	0.95314(8)
798 (III)	5.60996(3)	13.9688(1)	0.22241(5)	0.44949(14)	0.01934(16)	0.95388(9)

TABLE I. Cell parameters and atomic fractional coordinates of BiFeO_3 refined from Rietveld refinement in this study; Bi has fractional coordinates 0, 0, 0 (the value $z = 0$ was not set by symmetry, since the space group $R3c$ has no natural origin, but chosen to place the Bi atom at the origin of the unit cell), and Fe has fractional coordinates 0, 0, z . Standard deviations are given for the last significant figures in brackets. The Roman numerals beside the temperature values differentiate separate sequences on data, with two separate runs in the furnace (II and III) and one in the close-cycle refridgerator (I).

Refined values for the structural parameters for all temperatures are given in Tables I (unit cell and fractional coordinates) and II (atomic displacement parameters). The lattice parameters are plotted as functions of temperature in Figure 3. Both a and c vary smoothly with temperature, with no indications of anomalies or strain associated with the magnetic phase transition. The results for both a and c are consistent with previous results^{4,14}. Both lattice parameters show the usual change from linear variation with temperature at around 150 K. As discussed in the Section I, this region has previously been suggested to correspond to potential changes in the magnetic and/or atomic structures, and anomalous phonon behaviour. However, no apparent effects are seen in the data presented in Figure 3.

IV. ANALYSIS FROM THE REVERSE MONTE CARLO METHOD

A. RMC data refinement

The RMC fits to the three functions used in the RMC analysis, namely the Bragg scattering profile, the scattering function $i(Q)$, and the PDF $D(r)$, is shown for all temperatures in Figure 4. It can be seen that in all cases the quality of the fitting is good. It should be noted that the ripples in the experimental $i(Q)$ function were artificially created within the RMC method. Because the $D(r)$ function calculated from the RMC configuration has a maximum value of r , as set by the size of the configuration, the calculated $i(Q)$ function obtained by Fourier transform of $D(r)$ will contain truncation ripples. There-

T (K)	Bi U_{11}	Bi U_{12}	Bi U_{33}	Fe U_{iso}	O U_{11}	O U_{12}	O U_{13}	O U_{22}	O U_{23}	O U_{33}
16 (I)	0.19(3)	0.092(1)	0.05(5)	0.13(2)	-0.03(4)	0.06(4)	0.06(4)	0.30(5)	0.01(4)	0.34(4)
96 (I)	0.37(4)	0.184(1)	0.14(5)	0.21(3)	0.01(4)	0.07(4)	0.09(4)	0.34(5)	0.01(4)	0.42(4)
161 (I)	0.53(4)	0.267(2)	0.23(5)	0.29(3)	0.06(5)	0.08(5)	0.11(4)	0.37(5)	0.01(5)	0.52(5)
236 (I)	0.72(4)	0.361(2)	0.32(6)	0.38(3)	0.15(5)	0.09(5)	0.14(5)	0.41(5)	0.01(5)	0.68(5)
283 (I)	0.83(4)	0.416(2)	0.38(6)	0.43(3)	0.21(5)	0.10(5)	0.15(5)	0.44(5)	0.00(5)	0.76(5)
291 (III)	0.86(5)	0.431(2)	0.38(7)	0.41(3)	0.07(5)	0.00(5)	0.16(5)	0.29(6)	-0.01(5)	0.81(6)
294 (II)	0.90(4)	0.449(2)	0.41(6)	0.46(3)	0.20(5)	0.08(5)	0.16(5)	0.42(6)	0.00(5)	0.83(5)
373 (III)	1.11(5)	0.555(2)	0.56(7)	0.52(3)	0.27(5)	0.02(5)	0.17(5)	0.34(6)	-0.03(5)	1.02(6)
473 (III)	1.40(4)	0.700(2)	0.75(6)	0.62(3)	0.60(5)	0.06(5)	0.16(5)	0.43(5)	-0.09(5)	1.26(5)
572 (III)	1.68(3)	0.842(1)	0.96(5)	0.71(2)	1.10(4)	0.15(4)	0.08(4)	0.55(4)	-0.20(4)	1.45(4)
600 (II)	1.82(3)	0.912(1)	0.99(4)	0.77(2)	1.35(4)	0.29(4)	0.09(4)	0.73(4)	-0.20(3)	1.51(4)
627 (III)	1.81(3)	0.898(1)	1.04(4)	0.73(2)	1.53(4)	0.26(4)	0.00(4)	0.67(3)	-0.28(3)	1.44(4)
662 (III)	1.88(3)	0.939(1)	1.08(4)	0.75(2)	1.81(4)	0.32(4)	-0.06(4)	0.75(3)	-0.34(3)	1.41(4)
700 (II)	2.14(3)	1.070(1)	1.18(4)	0.86(2)	2.02(4)	0.44(4)	-0.02(4)	0.94(4)	-0.33(3)	1.60(4)
798 (III)	2.46(3)	1.228(1)	1.41(5)	0.93(2)	2.32(4)	0.38(4)	-0.12(5)	0.96(4)	-0.48(3)	1.81(4)

TABLE II. Atomic displacement parameters $100 \times U_{ij}$ (\AA^2) refined from Rietveld refinement. For Bi $U_{11} = U_{22}$, and $U_{13} = U_{23} = 0$. U_{ij} units are in \AA^2 . Standard deviations are given for the last significant figures in brackets. As in Table I the Roman numerals indicate the sets of data in different experimental runs.

fore to facilitate an accurate comparison between the calculated and experimental $i(Q)$ functions, the experimental $Q_i(Q)$ functions were automatically convolved with the Fourier transform of the box function of the same maximum value of r . For each temperature we performed ten independent RMC simulations, and all results are averaged over all final configurations.

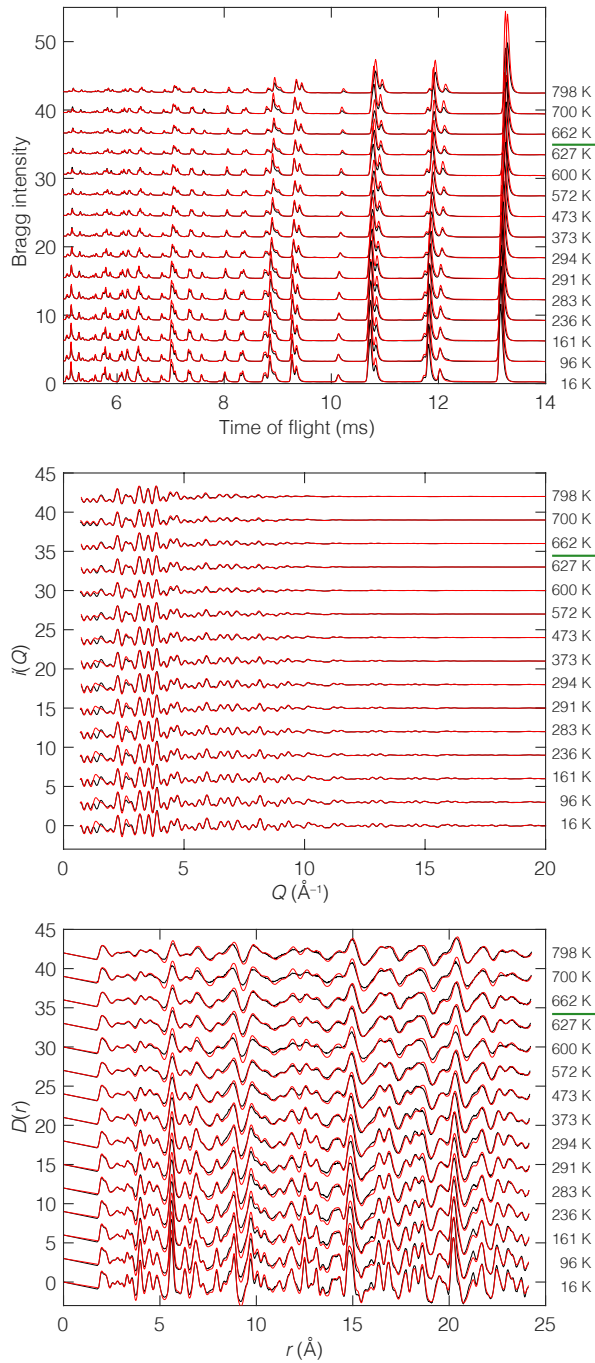


FIG. 4. Suite of data used in the Reverse Monte Carlo modelling, showing the Bragg diffraction data (top), total scattering data (middle) and pair distribution function (bottom). In each case the data are shown as black and the RMC calculation as red. Temperatures of the data are indicated on the right. In each graph data for different temperatures are vertically displaced sequentially by an equal amount. The horizontal lines in the temperature labels separate the temperatures in the magnetically ordered ($T > 630$ K) and disordered ($T < 630$ K) phases.

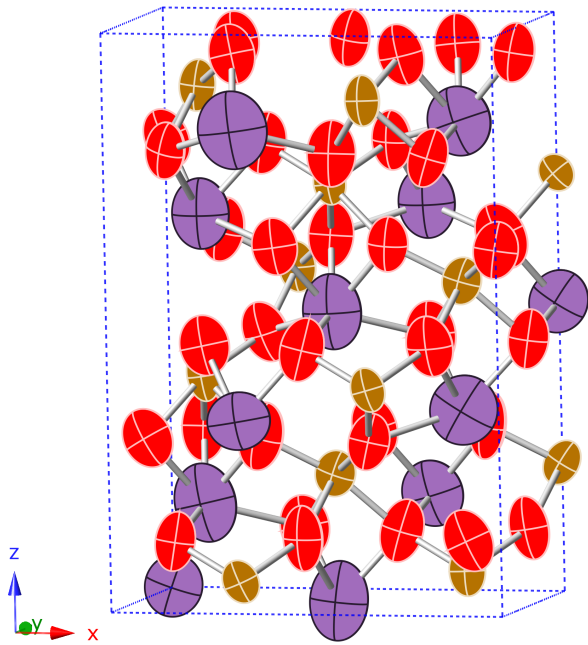


FIG. 5. Average structure with ellipsoid-shape atoms reflecting the amplitudes of anisotropic atomic vibrations at 473 K (Fe in orange, O in red and Bi in purple).

B. Average structure from RMC

We projected the position of all atoms in the configuration back into one unit cell, and from the distribution of atomic positions we calculated the average atomic positions and mean square anisotropic displacements from the associated distribution. An example of this projection, from the RMC analysis performed on the data collected at a temperature of 473 K, is shown in Figure 5. From the figure, and consistent with the results from Rietveld analysis shown in Table II, we can see that the atomic displacement parameters (which in this case represent thermal motions) of O and Bi atoms are larger than for the Fe atoms.

C. Local structure from RMC: atomic structures of the FeO_6 and BiO_{12} polyhedra

Here we focus on the fluctuations in the FeO_6 and BiO_{12} polyhedra. As the crystallographic analysis shows (above, and references 4 and 14), at all temperatures both polyhedra are significantly distorted from their highly symmetric form of the ideal cubic phase. The average local coordination of the Fe and Bi atoms is shown in Figure 6, where the distortions are clear. In particular, both polyhedra have lost their centre of symmetry and therefore have a local dielectric polarisation. In the case of the BiO_{12} polyhedra, not only is there a distortion of the shape but also a significant change in Bi–O distances,

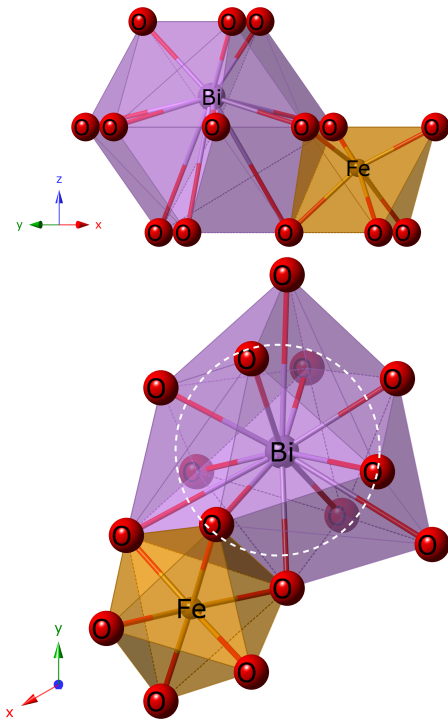


FIG. 6. Schematic illustration of FeO_6 and BiO_{12} polyhedra viewed along two axes. The white circle encompasses the shorter six Bi–O distances.

6 having shorter distances (2.2 and 2.5 Å) and 6 having longer distances (3.2 and 3.5 Å). This is consistent with asymmetric bonding expected for the BiO_{12} polyhedra as a result of hybridisation between the Bi $6s^2$ lone pair and the $6p$ orbitals⁴⁵.

Our analysis here is focussed on the orientations and lengths of the Fe–O and Bi–O bonds, how both their mean values and associated fluctuations change with temperature. The orientational distributions of the Fe–O and Bi–O bonds are shown as orthographic projections in Figures 7 and 8 respectively. These diagrams correspond to the vertical axis being parallel to the crystallographic [001], with separate diagrams showing views from positive and negative directions. Data are shown for four temperatures between 16–800 K. For both cases the diagrams include the two sets of symmetrically related bonds in different polyhedra. Thus we see pairs of peaks in the distribution functions. The advantage of showing both polyhedra in one diagram is that the angular separation between related pairs reflects the extent to which the symmetry of the parent cubic phase has been broken through bond and polyhedral reorientation (noting that both subtend the same angle with respect to the vertical axis, so the angular separation is directly about the vertical).

A striking point from Figures 7 and 8 is that the angular separations of the median bond orientations in the distribution functions for symmetrically-related pairs

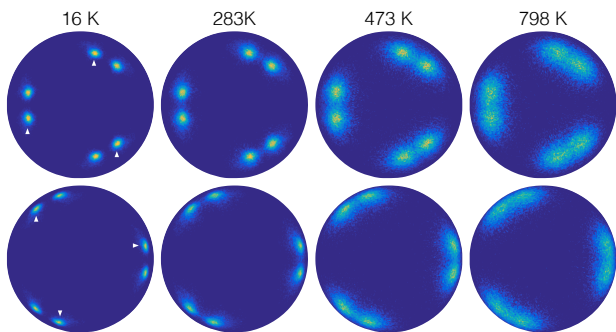


FIG. 7. Orthographic projection of the orientational distribution function of all Fe–O bonds in BiFeO_3 at four temperatures. Dark blue corresponds to no bonds in that orientation, and yellow shows the maximum value of the distribution function. The upper and lower plots show projections viewed down the $[001]$ and $[00\bar{1}]$ directions. The plots show vectors from two distinct but symmetrically-related orientations of the FeO_6 octahedra, meaning that the plots show 12 rather than 6 vectors. The peaks in the distribution function from one distinct set of octahedra are indicated by the white triangles in the plots for 16 K.

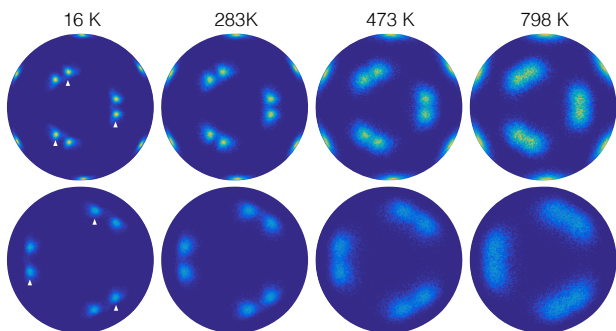


FIG. 8. Orthographic projection of the orientational distribution function of all Bi–O bonds in BiFeO_3 at four temperatures. The upper and lower plots show projections viewed down the $[001]$ and $[00\bar{1}]$ directions. As noted in the caption to Figure 7 the plots show vectors from two distinct but symmetrically-related orientations of the BiO_{12} cuboctahedra. As in Figure 7 we identify the peaks in the distribution function from one set of symmetrically identical cuboctahedra, but note that for the zenith angles just less than 90° the two distinct cuboctahedra have peaks with identical polar angles. This point can be seen by inspection of Figure 6.

change very little with temperature. This means that there are almost no changes in the mean orientations of either Fe–O or Bi–O bonds, and hence no rotations of the corresponding polyhedra, over the wide temperature range represented in the data. However, the extent of thermal motion associated with the orientations of the bonds grows considerably on heating, as seen in the wide angular distribution of the bond vectors. Indeed, the fluctuations become as large as the angular separation of the pairs of symmetrically-related peaks. We will comment

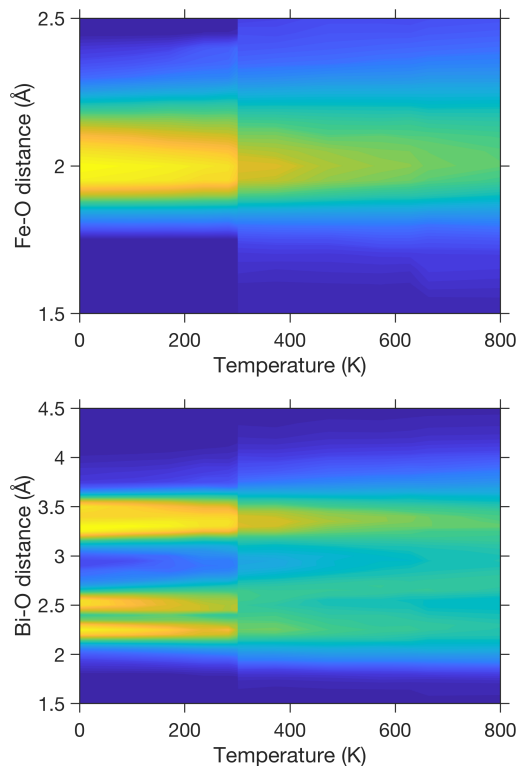


FIG. 9. Colour maps of the distributions of Fe–O and Bi–O distances. The difference in clarity between the low- and high-temperature data reflects the relatively high background from the furnace; see the discussion in the text.

more on this later in this section.

Second we consider the fluctuations in the bond distances. In Figure 9 we show a colour map of the distribution of Fe–O and Bi–O distances as a function of temperature. As an (important) aside, this figure shows one factor that we were unable to eliminate from our analysis, namely that the data obtained within the CCR and furnace show some systematic differences that feed through to slightly more disorder coming into the RMC configurations of the higher-temperature data. This probably arises from effects due to the relatively large background from the furnace.

In the case of the Fe–O bond, there are actually two symmetrically distinct distances of around 2.0 and 2.1 Å at low temperature, but with larger fluctuations than the difference in distances the overall distribution appears to be single-peaked in the colour map. On the other hand, there is a much wider spread of symmetrically distinct Bi–O distances, at around 2.3, 2.5, 3.3 and 3.5 Å. We plot the distribution functions for these four distinct bond distances for three temperatures in Figure 10. A similar broad distribution of Bi–O distances was seen in the room-temperature PDF study of $\text{BiFeO}_3\text{-PbTiO}_3$ solid solutions³⁰, and in La and La/Tb doped BiFeO_3 materials²⁴. Similar to the orientations of bond vectors,

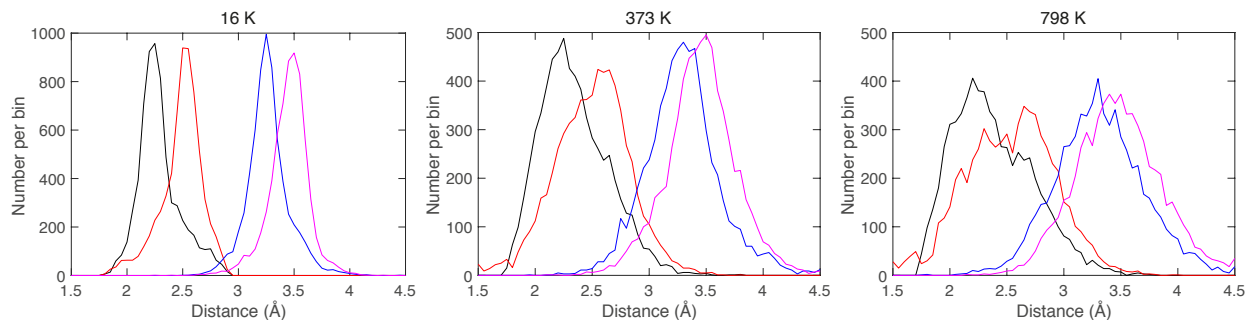


FIG. 10. Histograms of the four distinct Bi–O near-neighbour distances at three temperatures.

two points emerge from the histograms of instantaneous distances. First is that there is little change in the mid-points of the distribution of each bond distance over the whole temperature range, just as there is no clear change in the median values of the bond orientation distributions. Second is that there is a great deal of thermal motion. Indeed, the spread of distances at high temperature significantly exceeds the differences in mean positions.

Thus we see from taking all the data together that the average sizes, shapes and orientations of both types of coordination polyhedra remain virtually unchanged on heating from the lowest to highest temperature in this study. On the other hand, the same data show significant thermally-induced fluctuations, with the fluctuations becoming as large as the distortions of the average structure from the ideal cubic parent structure. This is consistent with the INS data, which show a considerable broadening of the peaks in the phonon density of states with increasing temperature, particularly for the modes associated with motions of the bismuth atoms^{46,47}, which might suggest the existence of significant anharmonicity. Likewise, resonant ultrasound spectroscopy has suggested increasing disorder with increasing temperature¹⁹.

There is one surprising aspect about the lack of change in the average structure across the temperature range of our data. Normally, on heating towards a phase transition to a higher-symmetry parent structure (in this case the relevant structure, in terms of symmetry group-subgroup relationships, is the γ phase of nominally cubic symmetry) the structure will transform towards that of the high-symmetry phase with the distortion becoming smaller on heating. Although one might argue that the highest temperature in our dataset falls short of the transition temperature by a considerable amount (300 K), in the sense of a second order Landau approximation (which is relevant in the case of ferroelectric phase transitions) where the ferroelectric distortions will vary with temperature as $(T - T_c)^{1/2}$, we might expect to see a reduction in the overall distortions by around 50%. This will not just be true for the dipolar displacements of the cations from the centres of their polyhedra, but also true of the distortions and rotations of the polyhedra. We can cite, for comparison, our previous RMC study of the phase

transition in SrTiO₃, which showed clearly changes upon heating towards the phase transition⁴⁸. The constancy of the structure across a wide range of temperatures is one of the curious aspects of the phase transition behaviour of BiFeO₃.

D. Local structure from RMC: dipolar fluctuations of the FeO₆ and BiO₁₂ polyhedra

In this final part we analyse the distortions of the FeO₆ and BiO₁₂ polyhedra in terms of local pseudo-dipole moments, calculated by summing over the bond vectors centred on the cation. What we call the “pseudo-dipole moment” is thus effectively the displacement of the central cation from the centroid of the polyhedron formed by its surrounding oxygen anions. This provides a convenient measure of the local moment without relying on any specific model of the charge distribution. The existence of these dipoles can be seen in the local structure diagrams in Figure 6. We calculated the size distributions of the pseudo-dipole moments in the [001] direction and in the orthogonal directions as functions of temperature, and present the results as colour maps in Figure 11.

The mean moment of the pseudo-dipole moments in the directions normal to [001] is zero as expected, and we see growing fluctuations of the pseudo-dipole moments on heating. On the other hand, there is a non-zero average moment for both polyhedra in the [001] direction, as is clearly seen in Figure 11. What is striking is that the mean pseudo-dipole moments of both types of polyhedra do not change significantly with temperature even though there is a significant effect of thermal motion. Indeed, the fluctuations are almost as large as the average moments at the highest temperature. The variances of the values of the pseudo-dipole moments of both polyhedra are shown in Figure 12, where we see a simple linear increase with temperature as normally expected for harmonic-like thermally-induced motions.

Finally we consider the distribution of orientations of the pseudo-dipole moments, which we show in orthographic projections in Figure 13. At lowest temperature it can be seen that the distribution is very tight, and the

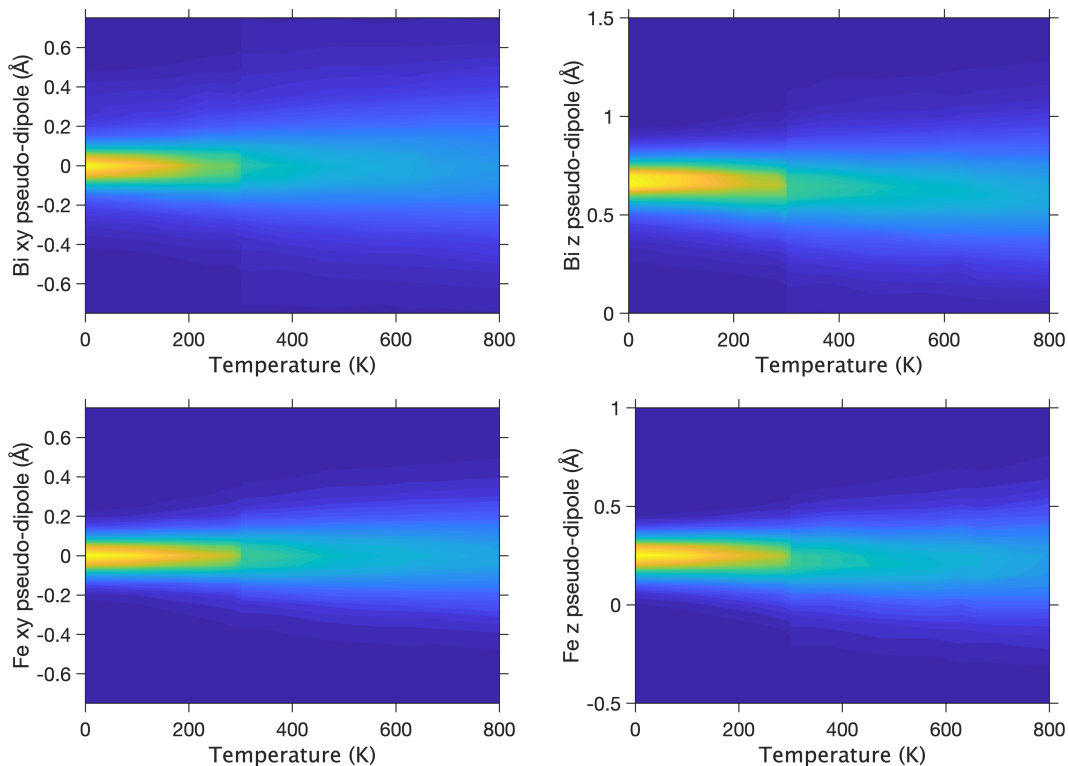


FIG. 11. Colour contour maps of the distributions of pseudo-dipole moments associated with the FeO_6 and BiO_{12} polyhedra. The dipole moments have units of \AA . As in Figure 9, the difference in clarity between the low- and high-temperature data reflects the relatively high background from the furnace.

shape of the distribution reflects slightly the three-fold symmetry of the crystal. However, on heating there is a wide distribution in the orientational distribution, even wider than the bond orientations, reflecting very large local fluctuations. This could be consistent with subtle fluctuations in structure as proposed in the inelastic neutron scattering data of reference 46.

V. CONCLUSION

The key result of this study is that the average atomic structure of BiFeO_3 remains robustly stable across the temperature range 16–800 K, in spite of the existence of large thermal fluctuations at the higher temperatures. This is represented in analysis of bond lengths, bond orientations, local coordination and local dipole moments. The RMC analysis in this study has shown that the local bonds around the Bi cation can fluctuate by a very large fraction, around 1 \AA with bond lengths of 2.5–3 \AA , yet the averages barely change. In the literature are several reports of apparent phase transitions and other thermal anomalies at various temperatures^{1,11,15–17,19,22}, but no structural anomalies are seen in this study in either the average or local structure. In this sense our results are consistent with the the results of several diffrac-

tion studies^{4,13,14}. In particular we see no effects from the magnetic phase transition in any of the features of the local structure. However, we note that no structural phase transition is expected at T_N with $R3c$ symmetry adopted both above and below T_N . Furthermore, there is no sign over the temperature range of this study of the onset of the phase transition on heating towards the paraelectric phase, such as a change in the local structure towards lower average distortion. Likewise, we see no evidence below room temperature to support either a structural phase transition or a significant change in the magnetic behaviour. Thus we conclude that all anomalies below room temperature reported in previous studies using indirect probes are unlikely to be seeing changes in the atomic structure of the bulk, or in local fluctuations, and thus are more likely to arise from effects generated at surfaces and interfaces (including domain walls and grain boundaries). Such effects would not have noticeable impacts on the scattering data and resultant PDF.

ACKNOWLEDGEMENTS

We are grateful to ISIS for provision of neutron beam time (project numbers RB1610460 and RB1310476). JD is grateful to the China Scholarship Council and Queen

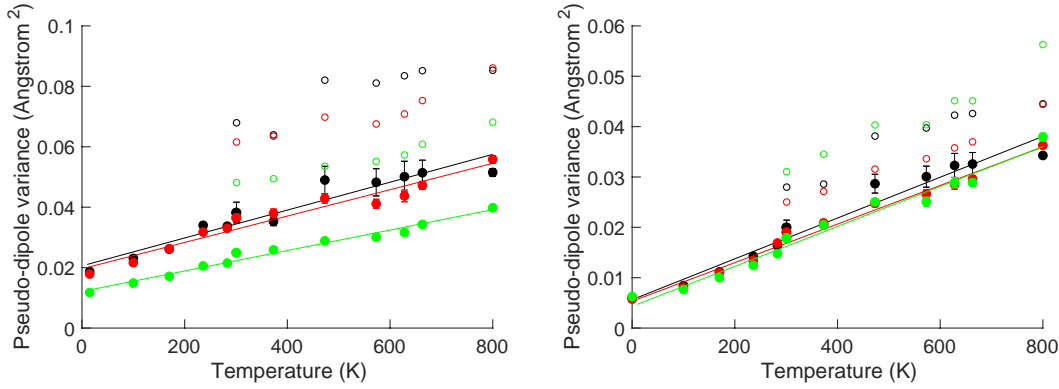


FIG. 12. Variances of the pseudo-dipole moments associated with the FeO_6 and BiO_{12} polyhedra. Black, red and green points correspond to directions x , y , z , where we expect the data for the x and y directions to have the same values. The open circles represent the RMC results without corrections. The filled circles below a temperature of 300 K are similarly the RMC results without corrections. The filled circles for temperatures above 300 K are obtained by subtracting from the RMC results a constant offset obtained by subtracting the difference in the two values at 300 K obtained for samples within the CCR and furnace, accounting for the problems described in the text in relation to Figure 9. The straight lines are guides to the eye to show that the corrected data are consistent with linear increases with temperature.

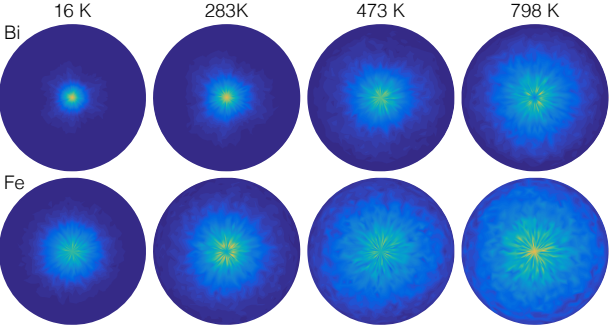


FIG. 13. Orthographic projection of the orientational distribution function of the local pseudo-dipoles associated with the BiO_{12} (top) and FeO_6 (bottom) polyhedral for four temperatures.

Mary University of London for financial support. This research utilised Queen Mary’s Apocrita HPC facility⁴⁹, supported by QMUL Research-IT and funded by EPSRC grants EP/K000128/1 and EP/K000233/1.

* Corresponding author: martin.dove@qmul.ac.uk

¹ G. Catalan and J. F. Scott, *Adv. Mater.* **21**, 2463 (2009).
² D. C. Arnold, *Ultrasonics, Ferroelec., Freq. Cont.* **62**, 62 (2015).
³ I. Sosnowska, T. Peterlin-Neumaier, and E. Steichele, *J. Phys. C* **15**, 4835 (1982).
⁴ D. C. Arnold, K. S. Knight, F. D. Morrison, and P. Lightfoot, *Phys. Rev. Lett.* **102**, 027602 (2009).
⁵ R. Palai, R. S. Katiyar, H. Schmid, P. Tissot, S. J. Clark, J. Robertson, S. A. T. Redfern, G. Catalan, and J. F. Scott, *Phys. Rev. B* **77**, 014110 (2008).
⁶ D. C. Arnold, K. S. Knight, G. Catalan, S. A. T. Redfern, J. F. Scott, P. Lightfoot, and F. D. Morrison, *Adv. Funct. Mater.* **20**, 2116 (2010).
⁷ S. M. Selbach, M. A. Einarsrud, and T. Grande, *Chemistry of Materials* **21**, 169 (2009).

⁸ T. Rojac, A. Bencan, B. Malic, G. Totuncu, J. L. Jones, J. E. Daniels, and D. Damjanovic, *Journal of the American Ceramic Society* **97**, 1993 (2014).
⁹ A. Perejón, P. E. Sánchez-Jimnez, J. M. Criado, and L. A. Pérez-Maqueda, *J. Phys. Chem. C* **116**, 26387 (2014).
¹⁰ D. C. Palmer, *Zeitschrift für Kristallographie - Crystalline Materials* **230**, 559 (2015).
¹¹ O. Delaire, M. B. Stone, J. Ma, A. Huq, D. Gout, C. Brown, K. F. Wang, and Z. F. Ren, *Phys. Rev. B* **85**, 064405 (2012).
¹² J. A. Schneeloch, Z. Xu, J. Wen, P. M. Gehring, C. Stock, M. Matsuda, B. Winn, G. Gu, S. M. Shapiro, R. J. Birgeneau, T. Ushiyama, Y. Yanagisawa, Y. Tomioka, T. Ito, and G. Xu, *Phys. Rev. B* **91**, 064301 (2015).
¹³ J. Herrero-Albillos, G. Catalan, J. A. Rodríguez-Velamazán, M. Viret, D. Coulson, and J. F. Scott, *J. Phys.: Condens. Matter.* **22**, 256001 (2010).

- ¹⁴ A. Palewicz, I. Sosnowska, R. Przenioslo, and A. W. Hewat, *Acta Physica Polonica A* **117**, 296 (2010).
- ¹⁵ M. Cazayous, Y. Gallais, A. Sacuto, R. de Sousa, D. Lebeugle, and D. Colson, *Phys. Rev. Lett.* **101**, 037601 (2008).
- ¹⁶ M. K. Singh, R. S. Katiyar, and J. F. Scott, *J. Phys. Condens. Matter* **20**, 252203 (2008).
- ¹⁷ B. Ramachandran, A. Dixit, R. Naik, and M. S. R. Rao, *J. Appl. Phys.* **110**, 104105 (2011).
- ¹⁸ J. Hlinka, J. Pokorny, S. Karimi, and I. M. Reaney, *Physical Review B* **83**, 020101(R) (2011).
- ¹⁹ R. Jarrier, X. Marti, J. Herrero-Albillos, P. Ferrer, R. Haumont, P. Gemeiner, G. Geneste, P. Berthet, T. Schulli, P. Cevc, R. Blinc, S. S. Wong, T. J. Park, M. Alexe, M. A. Carpenter, J. F. Scott, G. Catalan, and B. Dkhil, *Phys. Rev. B* **85**, 184104 (2012).
- ²⁰ N. Domingo, J. Narvaez, M. Alexe, and G. Catalan, *Journal of Applied Physics* **113**, 187220 (2013).
- ²¹ T. Yang, C. Wang, X. Zhang, Y. Feng, H. Guo, K. Jin, X. Gao, Z. Li, and X. Li, *Applied Physics Letters* **105**, 202901 (2014).
- ²² J. W. Lin, J. S. Gardner, C.-W. Wang, G. Deng, C. M. Wu, V. K. Peterson, and J. G. Lin, *AIP Adv.* **7**, 055836 (2017).
- ²³ B. Jiang and S. M. Selbach, *J. Solid State Chem.* **250**, 75 (2017).
- ²⁴ Y. Yoneda, K. Yoshii, S. Kohara, S. Kitagawa, and S. Mori, *Jpn. J. Appl. Phys.* **47**, 7590 (2008).
- ²⁵ Y. Yoneda, K. Yoshii, H. Saitoh, and J. Mizuki, *Ferroelectrics* **355**, 119 (2007).
- ²⁶ S. Unruan, M. Unruan, T. Monnor, S. Priya, and R. Yimnirun, *J. Am. Ceram. Soc.* **98**, 3291 (2015).
- ²⁷ N. Ishimatsu, T. Watanabe, K. Oka, M. Azuma, M. Mizumaki, K. Nitta, T. Ina, and N. Kawamura, *Phys. Rev. B* **92**, 054108 (2015).
- ²⁸ S. Unruan, S. Srilomsak, S. Priya, P. Jantaratana, S. Rujirawat, and R. Yimnirun, *Ceram. Int.* **41**, 4087 (2015).
- ²⁹ Y. Yoneda, Y. Kitanaka, Y. Noguchi, and M. Miyayama, *Phys. Rev. B* **86**, 184112 (2012).
- ³⁰ I. Levin, V. Krayzman, M. G. Tucker, and J. C. Woicik, *App. Phys. Lett.* **104**, 252913 (2015).
- ³¹ D. C. Arnold, K. S. Knight, F. D. Morrison, and P. Lightfoot, *Phys. Rev. Lett.* **102**, 027602 (2009).
- ³² A. C. Hannon, *Nuclear Instruments and Methods in Physics Research Section A: Accelerators, Spectrometers, Detectors and Associated Equipment* **551**, 88 (2005).
- ³³ M. T. Dove, A. E. Phillips, J. Du, D. A. Keen, D. C. Arnold, and M. G. Tucker, “Total scattering from multiferroic bismuth ferrite,” (2013), sTFC ISIS Neutron and Muon Source, DOI: 0.5286/ISIS.E.RB1310476.
- ³⁴ M. T. Dove, A. E. Phillips, J. Du, D. A. Keen, D. C. Arnold, and M. G. Tucker, “Total scattering from multiferroic bismuth ferrite at high temperatures,” (2016), sTFC ISIS Neutron and Muon Source, DOI: 0.5286/ISIS.E.RB1610460.
- ³⁵ O. Arnold, J. Bilheux, J. Borreguero, A. Buts, S. Campbell, L. Chapon, M. Doucet, N. Draper, R. F. Leal, M. Gigg, V. Lynch, A. Markvardsen, D. Mikkelson, R. Mikkelson, R. Miller, K. Palmen, P. Parker, G. Passos, T. Perring, P. Peterson, S. Ren, M. Reuter, A. Savici, J. Taylor, R. Taylor, R. Tolchenov, W. Zhou, and J. Zikovsky, *Nuclear Instruments and Methods in Physics Research Section A: Accelerators, Spectrometers, Detectors and Associated Equipment* **764**, 156 (2014).
- ³⁶ A. C. Larson and R. B. V. Dreele, *Los Alamos National Laboratory Report LAUR* **86**, 748 (2001).
- ³⁷ B. H. Toby, *Journal of Applied Crystallography* **34**, 210 (2001).
- ³⁸ A. K. Soper, *Rutherford Appleton Laboratory Technical Report RAL-TR* **13** (2011).
- ³⁹ A. C. Hannon, W. S. Howells, and A. K. Soper, in *Institute of Physics Conference Series* (2019) pp. 193–211.
- ⁴⁰ E. Lorch, *Journal of Physics C: Solid State Physics* **2**, 229 (1969).
- ⁴¹ E. Lorch, *Journal of Physics C: Solid State Physics* **3**, 1314 (1970).
- ⁴² M. G. Tucker, D. A. Keen, M. T. Dove, A. L. Goodwin, and Q. Hui, *Journal of Physics: Condensed Matter* **19**, 335218 (2007).
- ⁴³ Window ranges used were 3.5–4.66 Å for Fe–Fe, 1.76–2.5 Å for Fe–O, 2.5–4.7 Å for Fe–Bi, 1.75–5 Å for Bi–O, 2–5 Å for O–O and 3.3–4.8 Å for Bi–Bi.
- ⁴⁴ J. Herrero-Albillos, G. Catalan, J. A. Rodriguez-Velamazán, M. Viret, D. Colson, and J. F. Scott, *Journal of Physics: Condensed Matter* **22**, 256001 (2010).
- ⁴⁵ J.-G. Park, M. D. Le, J. Jeong, and S. Lee, *Journal of Physics: Condensed Matter* **26**, 433202 (2014).
- ⁴⁶ O. Delaire, M. B. Stone, J. Ma, A. Huq, D. Gout, C. Brown, K. F. Wang, and Z. F. Ren, *Phys. Rev. B* **85**, 064405 (2012).
- ⁴⁷ M. Zbiri, H. Schober, N. Choudhury, R. Mittal, S. L. Chaplot, S. J. Patwe, S. N. Achary, and A. K. Tyagi, *Applied Physics Letters* **100**, 142901 (2012).
- ⁴⁸ Q. Hui, M. G. Tucker, M. T. Dove, S. A. Wells, and D. A. Keen, *Journal of Physics: Condensed Matter* **17**, S111 (2005).
- ⁴⁹ T. King, S. Butcher, and L. Zalewski, *Apocrita - High Performance Computing Cluster for Queen Mary University of London* (2017).